

pubs.acs.org/NanoLett Letter

# Revealing High-Temperature Reduction Dynamics of High-Entropy Alloy Nanoparticles via In Situ Transmission Electron Microscopy

Boao Song, Yong Yang, Timothy T. Yang, Kun He, Xiaobing Hu, Yifei Yuan, Vinayak P. Dravid, Michael R. Zachariah,\* Wissam A. Saidi,\* Yuzi Liu,\* and Reza Shahbazian-Yassar\*

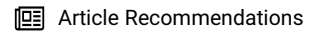


Cite This: Nano Lett. 2021, 21, 1742–1748



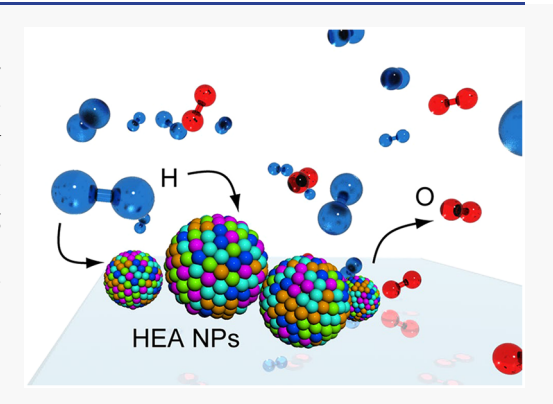
**ACCESS** 

Metrics & More



Supporting Information

ABSTRACT: Understanding the behavior of high-entropy alloy (HEA) materials under hydrogen (H<sub>2</sub>) environment is of utmost importance for their promising applications in structural materials, catalysis, and energy-related reactions. Herein, the reduction behavior of oxidized FeCoNiCuPt HEA nanoparticles (NPs) in atmospheric pressure H<sub>2</sub> environment was investigated by *in situ* gas-cell transmission electron microscopy (TEM). The reduction reaction front was maintained at the external surface of the oxide. During reduction, the oxide layer expanded and transformed into porous structures where oxidized Cu was fully reduced to Cu NPs while Fe, Co, and Ni remained in the oxidized form. *In situ* chemical analysis showed that the expansion of the oxide layer resulted from the outward diffusion flux of all transition metals (Fe, Co, Ni, Cu). Revealing the H<sub>2</sub> reduction behavior of HEA NPs facilitates the development of advanced multicomponent alloys for applications targeting H<sub>2</sub> formation and storage, catalytic hydrogenation, and corrosion removal.



**KEYWORDS:** High-entropy alloys, nanoparticles, in situ TEM, reduction, phase segregation

## **■ INTRODUCTION**

High-entropy alloys (HEAs) have attracted significant attention in recent years. <sup>1–4</sup> Because of the built-in high entropy effect from the atomically mixed more than five elements, HEAs exhibit unique characteristics in mechanical properties, thermal stability, and oxidation/corrosion resistance. <sup>2–5</sup> While extensive research efforts have been focused on the fabrication of bulk HEAs through solid-state processing, <sup>6–8</sup> bulk melting, <sup>9,10</sup> and additive manufacturing, <sup>1,11,12</sup> the recent advances in synthesizing single-phase HEA nanoparticles (HEA NPs) have expanded their applications in catalysis, electronics, and energy-related applications. Recently, carbothermal shock, <sup>13</sup> aerosol, <sup>14</sup> and fast moving bed pyrolysis <sup>15</sup> methods are shown to provide scalable quantities of HEA NPs for large-scale applications with high uniformity of atomic distribution and controllable size ranges.

In many potential applications of HEA NPs, the materials are exposed to oxidizing and reducing environments. For instance, as one of the most common reducing agents in chemical reactions, understanding the behavior of HEAs in H<sub>2</sub> environment is key for the future development of advanced materials. To date, HEAs have been investigated for their hydrogen embrittlement, <sup>16–19</sup> hydrogen storage, <sup>20,21</sup> hydrogenation, <sup>22,23</sup> and water splitting properties. <sup>24</sup> However, little is known on how HEAs behave in reducing environmental conditions. Currently, several studies on the oxidation of bulk HEAs in air <sup>25–30</sup> have identified different reaction kinetics including linear and parabolic for various compositions at high temperatures. The

authors recently reported the oxidation of HEA NPs under dried air at 400 °C and showed that Kirkendall effect governed the logarithmic behavior of the oxide layer growth kinetics.<sup>31</sup> Here, we used in situ closed-cell atmospheric pressure transmission electron microscopy<sup>32-44</sup> to study the high-temperature reduction behavior of oxidized FeCoNiCuPt HEA NPs in H<sub>2</sub> environment. In our study, closed-gas cell design<sup>37–43,45</sup> based on microfabricated devices was used to expose the NPs to atmospheric pressure H<sub>2</sub> at 400 °C. In order to investigate the local structural and chemical evolution in the NPs, in situ highangle annular dark-field (HAADF), annular bright-field (ABF) imaging, and energy dispersive spectroscopy (EDS) were used. In the H<sub>2</sub> reducing environment, the oxide layer over HEA NPs expanded and transformed to porous structure as H2 reacted with oxygen. Oxidized Cu was fully reduced to Cu NPs while Fe, Co, and Ni remained in their oxidized form. The H<sub>2</sub> reduction resulted in significant morphological and chemical changes where the core of the NPs reduced in size while the oxide shell was expanded with Cu NPs forming at outermost oxide surfaces.

Received: November 18, 2020 Revised: February 4, 2021 Published: February 11, 2021





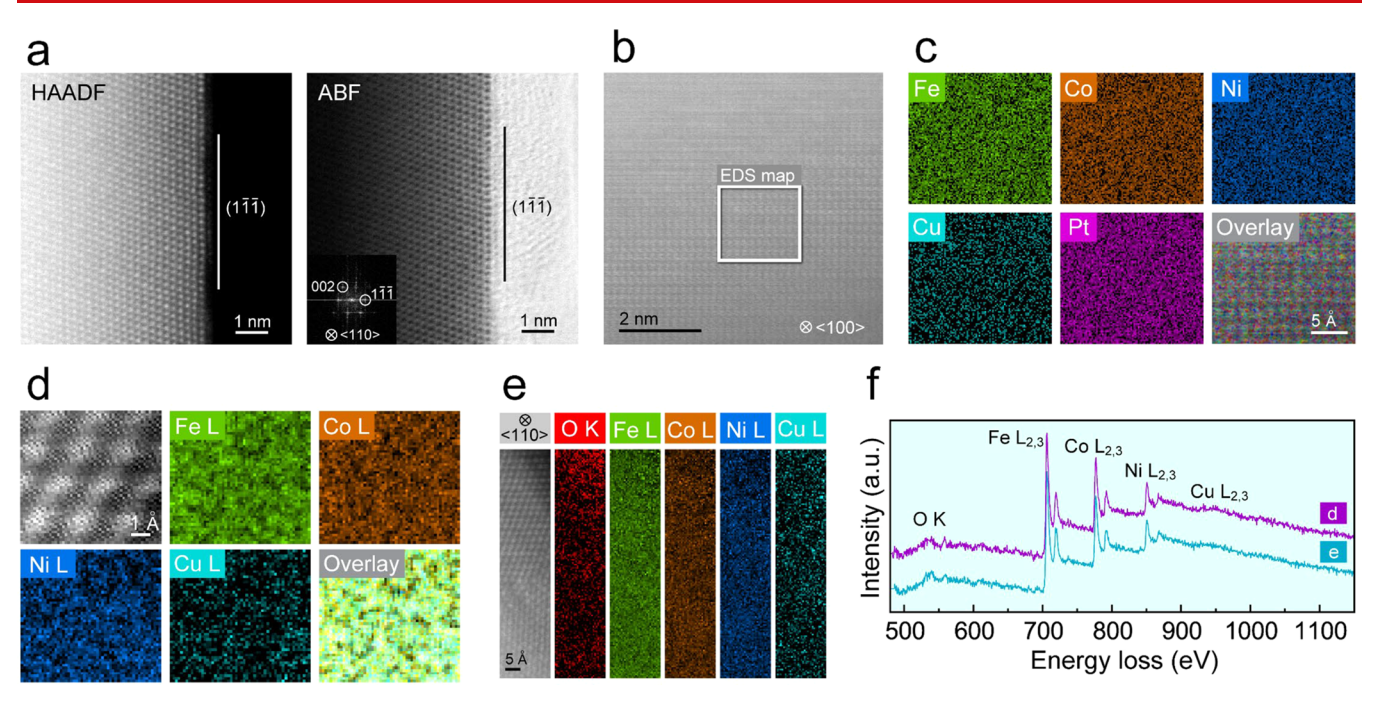


Figure 1. Electron microscopy characterization of HEA NPs on atomic structure and chemical composition. (a) The HAADF and ABF images show the atomic structure of as-prepared HEA in the  $\langle 110 \rangle$  zone axis. Inset in ABF image shows the FFT with (111) and (002) planes highlighted. (b) The HAADF image from the  $\langle 100 \rangle$  zone axis of HEA NP with the EDS map region highlighted in the box. (c) Atomic resolution EDS maps from boxed region in panel b showing all five elements and the overlaid image. (d) The atomic resolution EELS map showing atoms in the  $\langle 110 \rangle$  zone axis and corresponding Fe, Co, Ni, and Cu maps. (e) The EELS map from another region in the  $\langle 110 \rangle$  zone axis HEA NP extracted from O K-edge and Fe, Co, Ni, Cu L-edges. (f) The EEL spectra from the region in panels d and e.

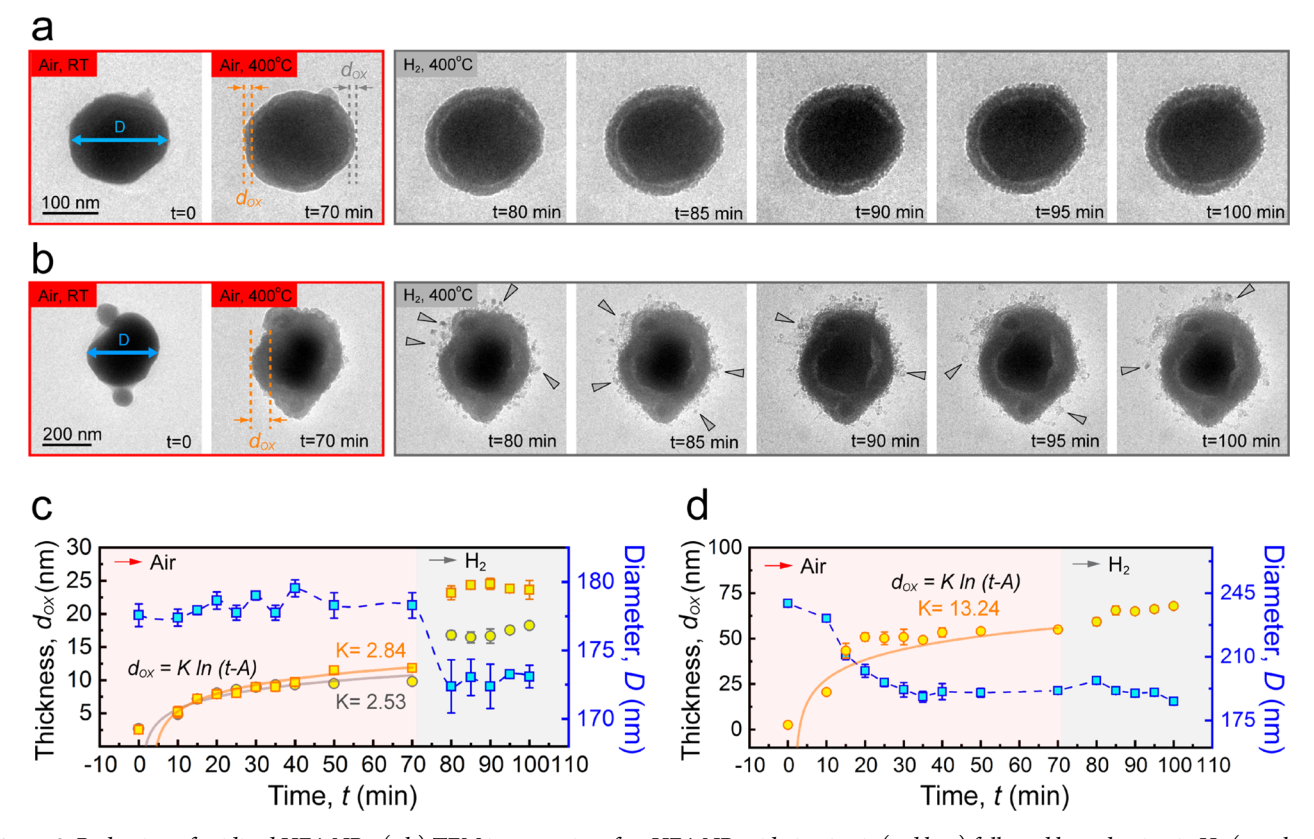


Figure 2. Reduction of oxidized HEA NPs. (a,b) TEM image series of an HEA NP oxidation in air (red box) followed by reduction in  $H_2$  (gray box). The temperature is RT in the first frame and 400 °C in all other frames. (c,d) Evolution of the oxide thickness  $d_{OX}$  and HEA NP diameter D during oxidation and reduction. As marked in panels a and b, the diameter D is shown in blue while oxide thickness  $d_{OX}$  is shown in orange (and gray) in left (and right) directions.

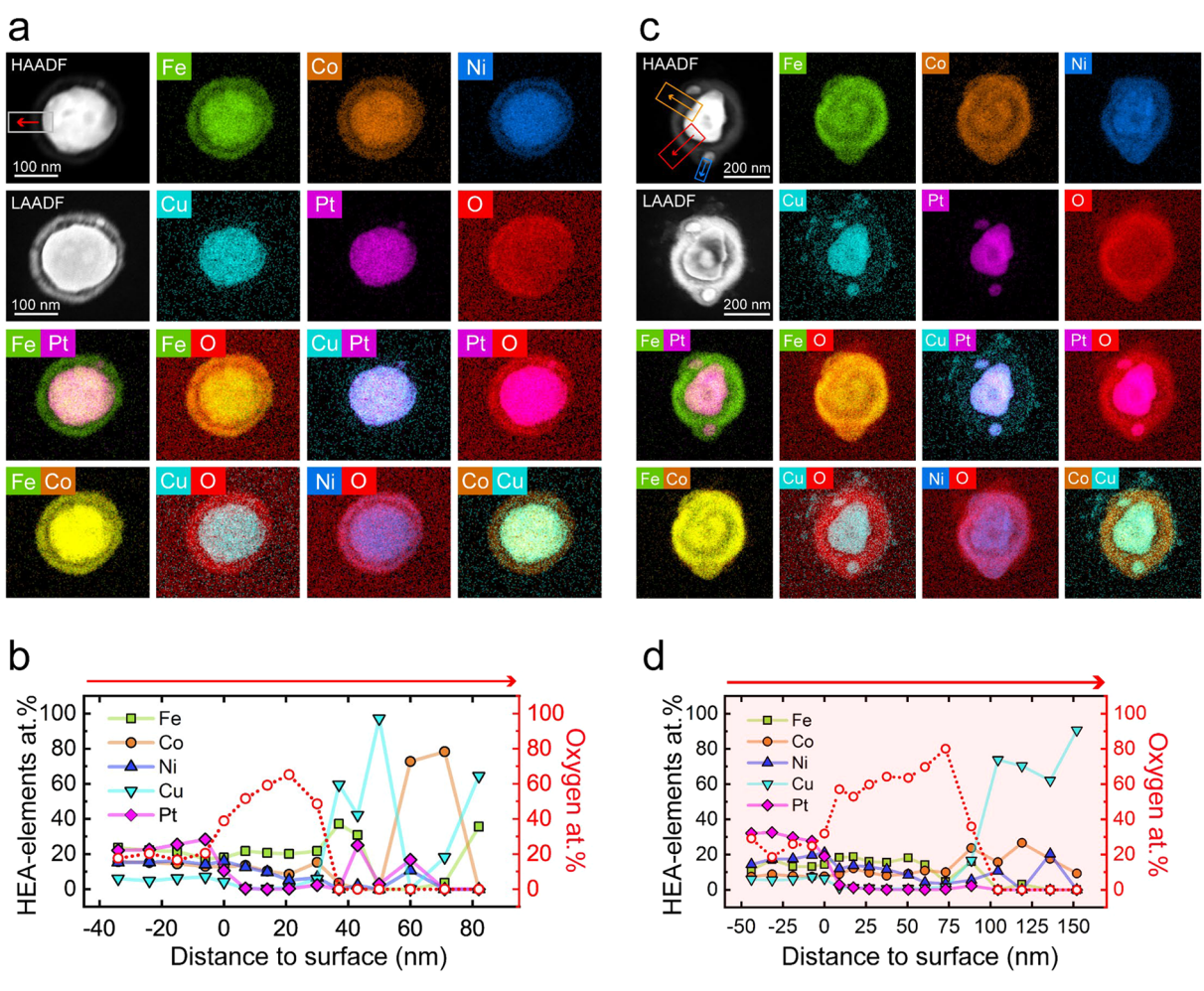


Figure 3. STEM-EDS of HEA NPs collected after *in situ* reduction. (a,c) STEM (HAADF and LAADF) images of HEA NP shown in Figure 2a,b, EDS maps of metal elements and O as well as selected overlaid EDS maps. (b,d) Atomic percentage distribution of metal elements and O. The arrows point to the directions in the same manner as marked in the HAADF image in panels a and c.

## RESULTS

The morphology and composition of the synthesized HEA NPs were characterized by X-ray powder diffraction (XRD), SEM, and TEM in our previous work, 14,31 where the average composition was shown to be  $Fe_{0.28}Co_{0.21}Ni_{0.20}Cu_{0.08}Pt_{0.23}$  for all size ranges. Here, we provide additional atomic resolution STEM imaging combined with STEM-EDS and STEM-electron energy loss spectrum (EELS) to confirm the chemical homogeneity at the atomic level. Figure 1a shows HAADF and ABF images of HEA NP along (110) zone axis in a facecentered cubic (fcc) crystal structure. Atomic resolution STEM-EDS maps from the  $\langle 100 \rangle$  zone axis of an NP (Figure 1b) shown in Figure 1c suggest homogeneous mixing of the five elements. In addition, atomic resolution STEM-EELS maps (Figure 1d) on an NP in the (110) zone axis further confirm the homogeneous distribution. Although the contrast of native oxide in the STEM images is not very obvious, the O K-edge map in Figure 1e shows more oxygen presence closer to the particle surface originating from the native oxide. The EEL spectra from regions in Figure 1d,e are then extracted and compared in Figure 1f. The two spectra are almost identical showing the O K-edge and L2.3-edges from transition metals, confirming the homogeneity in elemental distribution.

Next, in situ reduction on the HEA NPs was performed in TEM. First, a reduction step was carried out directly on the

pristine HEA NPs, but this resulted in no appreciable changes in the surface structures (Figure S1a,b). Hybrid Monte Carlo and molecular dynamics calculations using first-principles density functional theory<sup>46</sup> were also in agreement that hydrogen interactions with the surface do not induce any surface segregation phenomenon (Figure S1c) in contrast to the case of oxygen.<sup>31</sup> Then, a two-step process is conducted (Figure S2): the HEA NPs were first oxidized in atmospheric air (red box) and then reduced in H<sub>2</sub> environment (gray box). The individual HEA NP at the bottom left and the three HEA NPs at the top are magnified and displayed separately in Figure 2a,b. To confirm oxidation of HEA NPs, energy-filtered transmission electron microscopy (EFTEM) was performed. At t = 40 min in the frame in Figure S2, the EFTEM maps shown in Figure S3 include the Fe L-edge, O K-edge, and the overlaid image, suggesting that Fe diffuses out to contribute to the oxide growth. The maps for other metals are not shown due to a decreased signal-to-noise ratio as their L-edge onset is at a higher energy range. Within 10 min of the reduction process in H<sub>2</sub> (first frame in gray box, t = 80 min) both oxide layers on the smaller and larger NPs transform from dense to porous structure with cracks at the interface between the oxides and the HEA core. Also, the oxide layer is not fully reduced to metallic phase but only the external surface becomes porous, indicating the reaction front being close to the outer surface. It is also interesting to note that

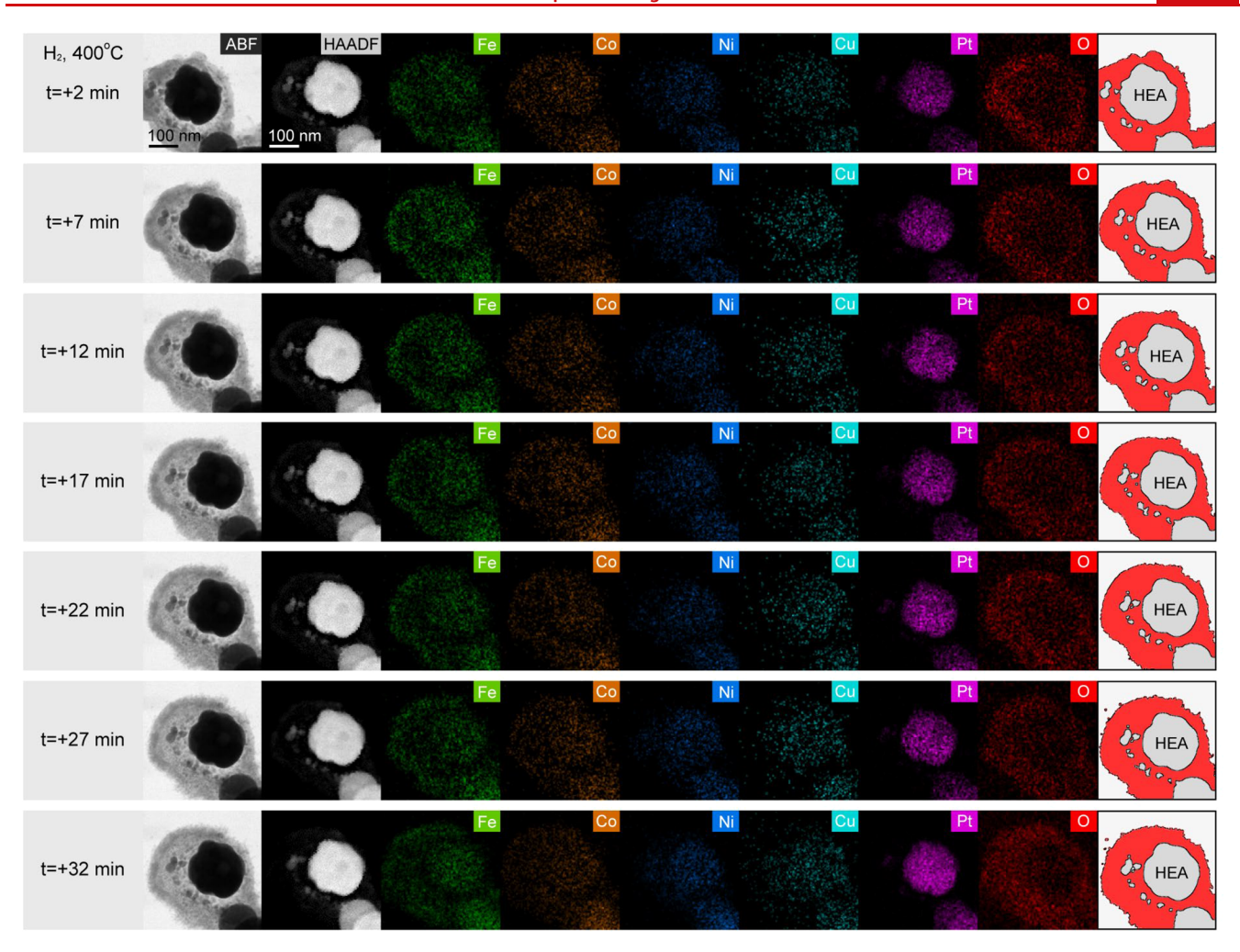
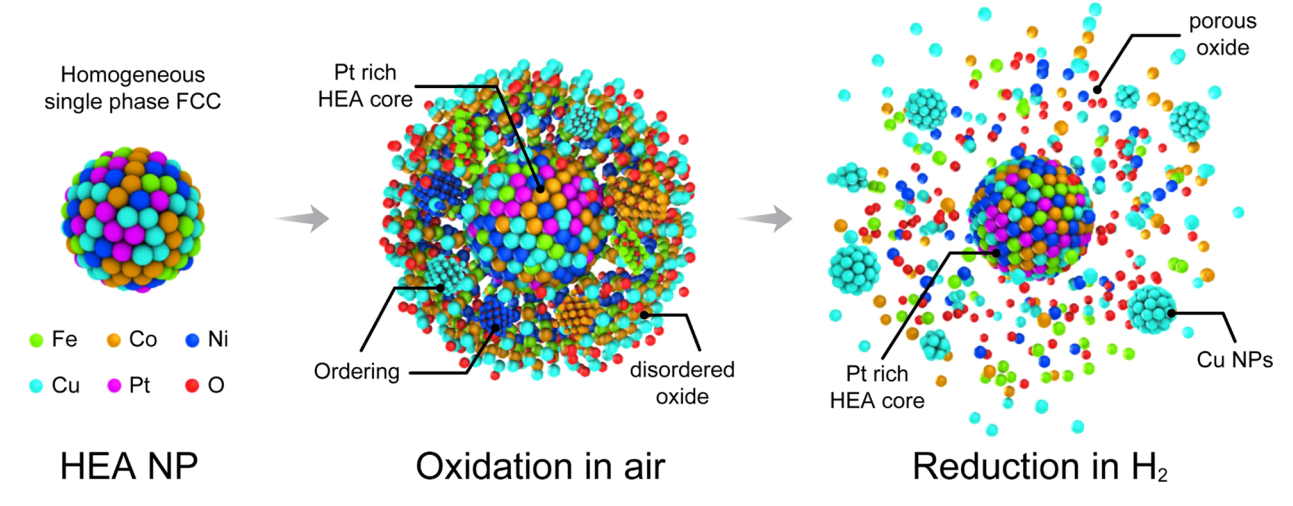


Figure 4. In situ EDS maps collected during the reduction HEA NPs in  $H_2$  right after oxidation. First column: time stamp; t = 0 is the time when the sample environment changed from air to  $H_2$ . Second column: the ABF and HAADF images of the reduction of HEA NPs in  $H_2$  and EDS maps of each element. Last column: the evolution of HEA NPs and the oxides corresponding to ABF images.

a large number of NP seeds can be seen to form on the oxide external surface as highlighted by the gray arrows. These seeds, ranging from few to tens of nanometers, appear to be unstable as their location changes in time. Figure 2c,d shows the measurement of the oxide thickness ( $d_{OX}$ ) and NPs diameter (D) evolution during oxidation and reduction. Consistent with our previous work,<sup>31</sup> the oxidation kinetics follow logarithmic law with a rate constant K close to 2.7 for smaller NP and 13.3 for larger NP. During reduction, the oxide layer on the smaller NP in both directions expands from  $\sim$ 10 to  $\sim$ 20 nm in thickness after H<sub>2</sub> penetration, accompanied by shrinkage of the HEA core diameter from  $\sim$ 178 to  $\sim$ 173 nm. Similarly, the oxide layer expands from  $\sim$ 50 to  $\sim$ 70 nm and further shrinkage of the core of the larger HEA NP can be observed.

To understand the chemical composition of HEA NPs after reduction, the STEM-EDS mappings were performed (Figure 3). The maps in Figure 3a,c were collected at the same region as in Figure 2a,b. It is clear that after H<sub>2</sub> reduction, the HEA NPs segregated into a reduced size HEA core with all five elements and a porous oxide layer containing Fe, Co, Ni. The Cu element, which is shown to be present in the oxide after oxidation, <sup>31</sup> is not concentrated in the oxide after reduction but instead dispersed widely around the HEA core (Figure 3a), suggesting that the oxidized Cu has been mostly reduced by H<sub>2</sub>. In contrast, Fe, Co, and Ni are not fully reduced and are still preserved in the oxide

region. This is clear in Figure 3c where the NP seed features on the external surface of the oxide mainly consist of Cu element, while Fe, Co, and Ni display a homogeneous mixing within the oxide layer. These results indicate that Cu is the only element that has been fully reduced and segregated into Cu NPs from the oxide. The HEA core, although shrank in size, consists of all five metal elements. The distribution of elements representing the boxed region of the HAADF image is shown in Figure 3b,d. They further indicate that Fe, Co, and Ni are present both in and outside of the oxide, while Cu is only present in HEA core and outside of the oxide layer. This confirms that Cu has been reduced into metallic Cu and segregated outward from the external oxide surface. Atomic distributions from other regions in the HAADF image in Figure 3c show the same trend (details in Figure S4). Furthermore, the HEA core of the HEA NP in Figure 3c displays condensed Pt with atomic ratio more than 23.5% while a significant reduced amount of Fe (12%) and Co (8%) resulted from outward diffusion, which is not obvious on the small NPs shown in Figure 3a with the less significant void collapse (21% Pt, 22% Fe, 18% Co, 18% Ni, 7% Cu). These results suggest that during reduction all transition metals in the oxide react with  $H_2$  and result in the expansion of the oxide layer. Simultaneously, the HEA core contracts and collapses due to the transition metal and associated vacancies' outward diffusion, leaving a gap between HEA core and the oxide internal surface.



**Figure 5.** Schematic showing the reduction of oxidized HEA NPs at 400  $^{\circ}$ C. The oxidized HEA NPs have Pt rich HEA core with disordered oxide layer containing Fe, Co, Ni, Cu. During reduction in H<sub>2</sub>, HEA core shrinks due to transition metals' outward diffusion, with expansion of the oxide and segregation of oxidized Cu into reduced Cu NPs.

Next, in situ EDS was performed to assist in revealing the compositional evolution. The HEA NPs underwent similar experimental procedures: first they were oxidized in air at 400 °C (Figure S5) and then reduced in H<sub>2</sub> at the same temperature. The oxidation process has been discussed in our previous work where transition metal diffusions are fully confirmed,<sup>31</sup> and here the reduction process is shown in Movie S1. Figure 4 shows the EDS maps taken from HEA NPs. When the oxidized HEA NPs are exposed to H2, it is obvious that the oxide expands as transition metals are reduced. Additionally, a concentration gradient between the HEA core and oxide layer drives further outward diffusion, resulting in depletion of transition metals at the internal oxide surface but enrichment at the external oxide surface. Therefore, a deficiency of elements between the HEA core and the internal oxide surface is observed, resulting in further segregated HEA core and oxide shell configurations.

Combining the information from real-time imaging and analytical EDS, the behavior of oxidized FeCoNiCuPt HEA NPs in H<sub>2</sub> can be illustrated in Figure 5. During reduction, all transition metals in the oxide react with H2 and Cu can be fully reduced and further segregated into Cu NPs. Most Fe, Co, and Ni are still preserved in the oxide form. On the basis of the Ellingham diagrams, <sup>47</sup> Cu oxide is the least stable among other metal oxides at 400 °C and thus preferable to reduce. Because of the disordered character of the oxide confirmed in our previous work, <sup>31</sup> H<sub>2</sub> penetration into and water diffusion out of the oxide are difficult, <sup>48</sup> resulting in the reaction front being at the external surface of oxide and formation of porous structures only at regions close to the outer surface. In addition, due to different diffusivity of cation and anion during oxidation vacancy injection is a common process<sup>35</sup> that can lead to a porous structure of the oxide. However, upon reduction this process is not reversed and can be another explanation of why the boundary for reduction is maintained at the oxide shell. The expansion of the oxide layer and simultaneous shrinkage of the HEA core are expected to be due to a change of concentration gradient that drives further transition metals' diffusion, and condensation of vacancies resulting in a gap between the HEA core and the oxide internal surface. As a result, the final products are HEA cores surrounded by porous oxides containing oxidized Fe, Co, and Ni with further segregated metallic Cu NPs at the external oxide surface. Besides EDS, we believe future investigations utilizing STEM-EELS to

analyze the energy-loss near-edge fine structures of the metal elements<sup>31</sup> will provide more insight of the oxidation states after reduction.

## CONCLUSION

The present work provides in situ TEM investigation of oxidized HEA NPs during reduction in atmospheric  $\rm H_2$  at constant temperature of 400 °C. The oxide layer transformation into porous structures is observed as  $\rm H_2$  penetrates into the oxide layer but the reaction front mostly remains at the external surface of the oxide. Oxidized Cu can be fully reduced and further segregated into Cu NPs, while Fe, Co, and Ni remain in the oxide phase. Further expansion of the oxide layer and size reduction of HEA core during  $\rm H_2$  reduction were observed resulting in segregated HEA core and oxide shell. The present study facilitates an in-depth understanding of HEA reduction mechanisms under reducing environment, and can provide insights into designing high corrosion resistance alloys,  $\rm H_2$ -resilient structural materials, hydrogen storage materials, and durable catalysis.

## ASSOCIATED CONTENT

#### Supporting Information

The Supporting Information is available free of charge at https://pubs.acs.org/doi/10.1021/acs.nanolett.0c04572.

In situ EDS maps of HEA NPs during reduction in  $\rm H_2$  at 400 °C (MP4)

Materials and Methods; in situ TEM image series of HEA NP reduction in  $\rm H_2$  at 400 °C. (Figure S1); in situ TEM image series of HEA NPs oxidation in air and reduction in  $\rm H_2$  (Figure S2); TEM image and EFTEM maps of HEA NPs collected during oxidation (Figure S3); EDS linescan showing Fe, Co, Ni, Cu, Pt, and O atom % (Figure S4); in situ EDS maps of HEA NPs oxidation in air (Figure S5) (PDF)

## AUTHOR INFORMATION

## **Corresponding Authors**

Reza Shahbazian-Yassar — Department of Mechanical and Industrial Engineering, University of Illinois at Chicago,

- Chicago, Illinois 60607, United States; o orcid.org/0000-0002-7744-4780; Email: rsyassar@uic.edu
- Yuzi Liu Center for Nanoscale Materials, Argonne National Laboratory, Argonne, Illinois 60439, United States; orcid.org/0000-0002-8733-1683; Email: yuziliu@anl.gov
- Wissam A. Saidi Department of Mechanical Engineering and Materials Science, University of Pittsburgh, Pittsburgh, Pennsylvania 15261, United States; orcid.org/0000-0001-6714-4832; Email: alsaidi@pitt.edu
- Michael R. Zachariah Department of Chemical Engineering and Materials Science, University of California Riverside, Riverside, California 92521, United States; occid.org/0000-0002-4115-3324; Email: mrz@engr.ucr.edu

### **Authors**

- Boao Song Department of Mechanical and Industrial Engineering, University of Illinois at Chicago, Chicago, Illinois 60607, United States; orcid.org/0000-0003-3124-3235
- Yong Yang Department of Chemical and Biomolecular Engineering, University of Maryland, College Park, Maryland 20742, United States; Department of Chemical Engineering and Materials Science, University of California Riverside, Riverside, California 92521, United States; orcid.org/ 0000-0001-5169-1479
- Timothy T. Yang Department of Mechanical Engineering and Materials Science, University of Pittsburgh, Pittsburgh, Pennsylvania 15261, United States; orcid.org/0000-0002-5785-0511
- Kun He Department of Materials Science and Engineering, International Institute for Nanotechnology (IIN), Northwestern University Atomic and Nanoscale Characterization Experimental (NUANCE) Center, Northwestern University, Evanston, Illinois 60208, United States
- Xiaobing Hu Department of Materials Science and Engineering, International Institute for Nanotechnology (IIN), Northwestern University Atomic and Nanoscale Characterization Experimental (NUANCE) Center, Northwestern University, Evanston, Illinois 60208, United States; orcid.org/0000-0002-9233-8118
- Yifei Yuan Department of Mechanical and Industrial Engineering, University of Illinois at Chicago, Chicago, Illinois 60607, United States; oocid.org/0000-0002-2360-8794
- Vinayak P. Dravid Department of Materials Science and Engineering, International Institute for Nanotechnology (IIN), Northwestern University Atomic and Nanoscale Characterization Experimental (NUANCE) Center, Northwestern University, Evanston, Illinois 60208, United States; Occid.org/0000-0002-6007-3063

Complete contact information is available at: https://pubs.acs.org/10.1021/acs.nanolett.0c04572

## **Author Contributions**

B.S. and R.S.-Y. developed the idea for this project. Y.Y. and M.Z. synthesized the specimens. B.S. performed all the electron microscopy studies. T.Y. and W.S. performed the DFT studies. Y.L., K.H., X.H., Y.Y., and V.D. assisted the electron microscopy efforts. B.S. completed the writing of the manuscript under the supervision of R.S.-Y. All of the authors made contributions to the discussion and interpretation of results and modified parts of this paper.

#### **Notes**

The authors declare no competing financial interest.

### ACKNOWLEDGMENTS

R.S.-Y. is thankful to National Science Foundation (NSF) for Award No. DMR-1809439. W.S. is thankful to NSF for Award No. DMR-1809085. Part of the computational work is supported by the University of Pittsburgh Center for Research Computing. Part of this work is performed at the Center for Nanoscale Materials (CNM), which is a U.S. Department of Energy Office of Science User Facility, and supported by the U.S. Department of Energy, Office of Science, under Contract No. DE-AC02-06CH11357. We utilized JEOL JEM-ARM 200CF and JEOL JEM-3010 available at Electron Microscopy Center as part of RRC shared facility at UIC. The UIC JEOL JEM-ARM 200CF was obtained by a MRI-R2 grant from the NSF Award DMR-0959470. We are thankful to Dr. F. Shi from UIC for assisting and facilitating electron microscopy efforts. Some of the electron microscopy experiments were performed at the EPIC facility of Northwestern University's NUANCE Center with support from the Soft and Hybrid Nanotechnology Experimental (SHyNE) Resource (NSF ECCS-1542205); the MRSEC program (NSF DMR-1720139) at the Materials Research Center; the International Institute for Nanotechnology (IIN); the Keck Foundation; and the State of Illinois, through the IIN. Also, M.Z. appreciates the support of an ONR award through MURI program.

## REFERENCES

- (1) Brif, Y.; Thomas, M.; Todd, I. The Use of High-Entropy Alloys in Additive Manufacturing. *Scr. Mater.* **2015**, *99*, 93–96.
- (2) Chen, J.; Zhou, X.; Wang, W.; Liu, B.; Lv, Y.; Yang, W.; Xu, D.; Liu, Y. A Review on Fundamental of High Entropy Alloys with Promising High-Temperature Properties. *J. Alloys Compd.* **2018**, *760*, 15–30.
- (3) George, E. P.; Raabe, D.; Ritchie, R. O. High-Entropy Alloys. *Nature Reviews Materials* **2019**, 4, 515–534.
- (4) Tsai, M.-H.; Yeh, J.-W. High-Entropy Alloys: A Critical Review. *Mater. Res. Lett.* **2014**, *2*, 107–123.
- (5) Ye, Y. F.; Wang, Q.; Lu, J.; Liu, C. T.; Yang, Y. High-Entropy Alloy: Challenges and Prospects. *Mater. Today* **2016**, *19*, 349–362.
- (6) Fu, Z.; Chen, W.; Wen, H.; Zhang, D.; Chen, Z.; Zheng, B.; Zhou, Y.; Lavernia, E. J. Microstructure and Strengthening Mechanisms in an FCC Structured Single-Phase Nanocrystalline Co<sub>25</sub>Ni<sub>25</sub>Fe<sub>25</sub>Al<sub>7.5</sub>Cu<sub>17.5</sub> High-Entropy Alloy. *Acta Mater.* **2016**, *107*, 59–71.
- (7) Sriharitha, R.; Murty, B. S.; Kottada, R. S. Alloying, Thermal Stability and Strengthening in Spark Plasma Sintered Alxcocrcufeni High Entropy Alloys. *J. Alloys Compd.* **2014**, 583, 419–426.
- (8) Fang, S.; Chen, W.; Fu, Z. Microstructure and Mechanical Properties of Twinned Al<sub>0.5</sub>CrFeNiCo<sub>0.3</sub>C<sub>0.2</sub> High Entropy Alloy Processed by Mechanical Alloying and Spark Plasma Sintering. *Mater. Eng. (Reigate, U. K.)* **2014**, *54*, 973–979.
- (9) Yeh, J. W.; Chen, S. K.; Lin, S. J.; Gan, J. Y.; Chin, T. S.; Shun, T. T.; Tsau, C. H.; Chang, S. Y. Nanostructured High-Entropy Alloys with Multiple Principal Elements: Novel Alloy Design Concepts and Outcomes. *Adv. Eng. Mater.* **2004**, *6*, 299–303.
- (10) Otto, F.; Yang, Y.; Bei, H.; George, E. P. Relative Effects of Enthalpy and Entropy on the Phase Stability of Equiatomic High-Entropy Alloys. *Acta Mater.* **2013**, *61*, 2628–2638.
- (11) Fujieda, T.; Shiratori, H.; Kuwabara, K.; Kato, T.; Yamanaka, K.; Koizumi, Y.; Chiba, A. First Demonstration of Promising Selective Electron Beam Melting Method for Utilizing High-Entropy Alloys as Engineering Materials. *Mater. Lett.* **2015**, *159*, 12–15.
- (12) Gorsse, S.; Hutchinson, C.; Gouné, M.; Banerjee, R. Additive Manufacturing of Metals: A Brief Review of the Characteristic Microstructures and Properties of Steels, Ti-6Al-4V and High-Entropy Alloys. *Sci. Technol. Adv. Mater.* **2017**, *18*, 584–610.

- (13) Yao, Y.; Huang, Z.; Xie, P.; Lacey, S. D.; Jacob, R. J.; Xie, H.; Chen, F.; Nie, A.; Pu, T.; Rehwoldt, M.; Yu, D.; Zachariah, M. R.; Wang, C.; Shahbazian-Yassar, R.; Li, J.; Hu, L. Carbothermal Shock Synthesis of High-Entropy-Alloy Nanoparticles. *Science* **2018**, 359, 1489–1494.
- (14) Yang, Y.; Song, B.; Ke, X.; Xu, F.; Bozhilov, K. N.; Hu, L.; Shahbazian-Yassar, R.; Zachariah, M. R. Aerosol Synthesis of High Entropy Alloy Nanoparticles. *Langmuir* **2020**, *36*, 1985–1992.
- (15) Gao, S.; Hao, S.; Huang, Z.; Yuan, Y.; Han, S.; Lei, L.; Zhang, X.; Shahbazian-Yassar, R.; Lu, J. Synthesis of High-Entropy Alloy Nanoparticles on Supports by the Fast Moving Bed Pyrolysis. *Nat. Commun.* **2020**, *11*, 2016.
- (16) Zhao, Y.; Lee, D.-H.; Seok, M.-Y.; Lee, J.-A.; Phaniraj, M. P.; Suh, J.-Y.; Ha, H.-Y.; Kim, J.-Y.; Ramamurty, U.; Jang, J.-I. Resistance of CoCrFeMnNi High-Entropy Alloy to Gaseous Hydrogen Embrittlement. *Scr. Mater.* **2017**, *135*, 54–58.
- (17) Luo, H.; Li, Z.; Lu, W.; Ponge, D.; Raabe, D. Hydrogen Embrittlement of an Interstitial Equimolar High-Entropy Alloy. *Corros. Sci.* **2018**, *136*, 403–408.
- (18) Luo, H.; Lu, W.; Fang, X.; Ponge, D.; Li, Z.; Raabe, D. Beating Hydrogen with Its Own Weapon: Nano-Twin Gradients Enhance Embrittlement Resistance of a High-Entropy Alloy. *Mater. Today* **2018**, *21*, 1003–1009.
- (19) Kwon, Y. J.; Won, J. W.; Park, S. H.; Lee, J. H.; Lim, K. R.; Na, Y. S.; Lee, C. S. Ultrahigh-Strength CoCrFeMnNi High-Entropy Alloy Wire Rod with Excellent Resistance to Hydrogen Embrittlement. *Mater. Sci. Eng., A* **2018**, 732, 105–111.
- (20) Kunce, I.; Polanski, M.; Bystrzycki, J. Microstructure and Hydrogen Storage Properties of a TiZrNbMoV High Entropy Alloy Synthesized Using Laser Engineered Net Shaping (Lens). *Int. J. Hydrogen Energy* **2014**, *39*, 9904–9910.
- (21) Sahlberg, M.; Karlsson, D.; Zlotea, C.; Jansson, U. Superior Hydrogen Storage in High Entropy Alloys. *Sci. Rep.* **2016**, *6*, 36770.
- (22) Karlsson, D.; Ek, G.; Cedervall, J.; Zlotea, C.; Møller, K. T.; Hansen, T. C.; Bednarčík, J.; Paskevicius, M.; Sørby, M. H.; Jensen, T. R.; Jansson, U.; Sahlberg, M. Structure and Hydrogenation Properties of a HfNbTiVZr High-Entropy Alloy. *Inorg. Chem.* **2018**, *57*, 2103–2110.
- (23) Zlotea, C.; Sow, M. A.; Ek, G.; Couzinié, J. P.; Perrière, L.; Guillot, I.; Bourgon, J.; Møller, K. T.; Jensen, T. R.; Akiba, E.; Sahlberg, M. Hydrogen Sorption in TiZrNbHfTa High Entropy Alloy. *J. Alloys Compd.* **2019**, 775, 667–674.
- (24) Zhang, G.; Ming, K.; Kang, J.; Huang, Q.; Zhang, Z.; Zheng, X.; Bi, X. High Entropy Alloy as a Highly Active and Stable Electrocatalyst for Hydrogen Evolution Reaction. *Electrochim. Acta* **2018**, 279, 19–23.
- (25) Daoud, H. M.; Manzoni, A. M.; Völkl, R.; Wanderka, N.; Glatzel, U. Oxidation Behavior of Al<sub>8</sub>Co<sub>17</sub>Cr<sub>17</sub>Cu<sub>8</sub>Fe<sub>17</sub>Ni<sub>33</sub>, Al<sub>23</sub>Co<sub>15</sub>Cr<sub>23</sub>Cu<sub>8</sub>Fe<sub>15</sub>Ni<sub>15</sub>, and Al<sub>17</sub>Co<sub>17</sub>Cr<sub>17</sub>Cu<sub>17</sub>Fe<sub>17</sub>Ni<sub>17</sub> compositionally Complex Alloys (High-Entropy Alloys) at Elevated Temperatures in Air. Adv. Eng. Mater. 2015, 17, 1134–1141.
- (26) Kai, W.; Li, C. C.; Cheng, F. P.; Chu, K. P.; Huang, R. T.; Tsay, L. W.; Kai, J. J. Air-Oxidation of Feconicr-Based Quinary High-Entropy Alloys at 700–900 °C. Corros. Sci. 2017, 121, 116–125.
- (27) Butler, T. M.; Weaver, M. L. Oxidation Behavior of Arc Melted Alcocrfeni Multi-Component High-Entropy Alloys. *J. Alloys Compd.* **2016**, 674, 229–244.
- (28) Laplanche, G.; Volkert, U. F.; Eggeler, G.; George, E. P. Oxidation Behavior of the CrMnFeCoNi High-Entropy Alloy. *Oxid. Met.* **2016**, *85*, 629–645.
- (29) Gorr, B.; Azim, M.; Christ, H. J.; Mueller, T.; Schliephake, D.; Heilmaier, M. Phase Equilibria, Microstructure, and High Temperature Oxidation Resistance of Novel Refractory High-Entropy Alloys. *J. Alloys Compd.* **2015**, *624*, 270–278.
- (30) Kai, W.; Li, C. C.; Cheng, F. P.; Chu, K. P.; Huang, R. T.; Tsay, L. W.; Kai, J. J. The Oxidation Behavior of an Equimolar FeCoNiCrMn High-Entropy Alloy at 950°C in Various Oxygen-Containing Atmospheres. *Corros. Sci.* **2016**, *108*, 209–214.
- (31) Song, B.; Yang, Y.; Rabbani, M.; Yang, T. T.; He, K.; Hu, X.; Yuan, Y.; Ghildiyal, P.; Dravid, V. P.; Zachariah, M. R.; Saidi, W. A.; Liu,

- Y.; Shahbazian-Yassar, R. *In Situ* Oxidation Studies of High-Entropy Alloy Nanoparticles. *ACS Nano* **2020**, *14*, 15131–15143.
- (32) Xia, W.; Yang, Y.; Meng, Q.; Deng, Z.; Gong, M.; Wang, J.; Wang, D.; Zhu, Y.; Sun, L.; Xu, F.; Li, J.; Xin, H. L. Bimetallic Nanoparticle Oxidation in Three Dimensions by Chemically Sensitive Electron Tomography and *in Situ* Transmission Electron Microscopy. *ACS Nano* **2018**, *12*, 7866–7874.
- (33) Zhu, Y.; Sushko, P. V.; Melzer, D.; Jensen, E.; Kovarik, L.; Ophus, C.; Sanchez-Sanchez, M.; Lercher, J. A.; Browning, N. D. Formation of Oxygen Radical Sites on Movnbteox by Cooperative Electron Redistribution. *J. Am. Chem. Soc.* **2017**, *139*, 12342–12345.
- (34) Zou, L.; Li, J.; Zakharov, D.; Stach, E. A.; Zhou, G. *In Situ* Atomic-Scale Imaging of the Metal/Oxide Interfacial Transformation. *Nat. Commun.* **2017**, *8*, 307.
- (35) Wang, C.-M.; Genc, A.; Cheng, H.; Pullan, L.; Baer, D. R.; Bruemmer, S. M. In-Situ TEM Visualization of Vacancy Injection and Chemical Partition During Oxidation of Ni-Cr Nanoparticles. *Sci. Rep.* **2015**, *4*, 3683.
- (36) Jeangros, Q.; Hansen, T. W.; Wagner, J. B.; Damsgaard, C. D.; Dunin-Borkowski, R. E.; Hébert, C.; Van herle, J.; Hessler-Wyser, A. Reduction of Nickel Oxide Particles by Hydrogen Studied in an Environmental Tem. *J. Mater. Sci.* **2013**, *48*, 2893–2907.
- (37) Prestat, E.; Kulzick, M. A.; Dietrich, P. J.; Smith, M. M.; Tien, M. E. P.; Burke, M. G.; Haigh, S. J.; Zaluzec, N. J. *In Situ* Industrial Bimetallic Catalyst Characterization Using Scanning Transmission Electron Microscopy and X-Ray Absorption Spectroscopy at One Atmosphere and Elevated Temperature. *ChemPhysChem* **2017**, *18*, 2151–2156.
- (38) Jiang, Y.; Li, H.; Wu, Z.; Ye, W.; Zhang, H.; Wang, Y.; Sun, C.; Zhang, Z. *In Situ* Observation of Hydrogen-Induced Surface Faceting for Palladium-Copper Nanocrystals at Atmospheric Pressure. *Angew. Chem., Int. Ed.* **2016**, *55*, 12427–12430.
- (39) Tan, S. F.; Chee, S. W.; Baraissov, Z.; Jin, H.; Tan, T. L.; Mirsaidov, U. Real-Time Imaging of Nanoscale Redox Reactions over Bimetallic Nanoparticles. *Adv. Funct. Mater.* **2019**, *29*, 1903242.
- (40) Altantzis, T.; Lobato, I.; De Backer, A.; Béché, A.; Zhang, Y.; Basak, S.; Porcu, M.; Xu, Q.; Sánchez-Iglesias, A.; Liz-Marzán, L. M.; Van Tendeloo, G.; Van Aert, S.; Bals, S. Three-Dimensional Quantification of the Facet Evolution of Pt Nanoparticles in a Variable Gaseous Environment. *Nano Lett.* **2019**, *19*, 477–481.
- (41) Dembélé, K.; Bahri, M.; Melinte, G.; Hirlimann, C.; Berliet, A.; Maury, S.; Gay, A. S.; Ersen, O. Insight by *in Situ* Gas Electron Microscopy on the Thermal Behaviour and Surface Reactivity of Cobalt Nanoparticles. *ChemCatChem* **2018**, *10*, 4004–4009.
- (42) Song, B.; Yang, T. T.; Yuan, Y.; Sharifi-Asl, S.; Cheng, M.; Saidi, W. A.; Liu, Y.; Shahbazian-Yassar, R. Revealing Sintering Kinetics of MoS<sub>2</sub>-Supported Metal Nanocatalysts in Atmospheric Gas Environments *via* Operando Transmission Electron Microscopy. *ACS Nano* **2020**, *14*, 4074–4086.
- (43) Xin, H. L.; Niu, K.; Alsem, D. H.; Zheng, H. *In Situ* TEM Study of Catalytic Nanoparticle Reactions in Atmospheric Pressure Gas Environment. *Microsc. Microanal.* **2013**, *19*, 1558–1568.
- (44) Baldi, A.; Narayan, T. C.; Koh, A. L.; Dionne, J. A. *In Situ* Detection of Hydrogen-Induced Phase Transitions in Individual Palladium Nanocrystals. *Nat. Mater.* **2014**, *13*, 1143–1148.
- (45) He, B.; Zhang, Y.; Liu, X.; Chen, L. In-Situ Transmission Electron Microscope Techniques for Heterogeneous Catalysis. *ChemCatChem* **2020**, *12*, 1853–1872.
- (46) Widom, M.; Huhn, W. P.; Maiti, S.; Steurer, W. Hybrid Monte Carlo/Molecular Dynamics Simulation of a Refractory Metal High Entropy Alloy. *Metall. Mater. Trans. A* **2014**, *45*, 196–200.
- (47) Turkdogan, E. T. Physical Chemistry of High Temperature Technology; Academic Press: United Kingdom, 1980.
- (48) Richardson, J. X-Ray Diffraction Study of Nickel Oxide Reduction by Hydrogen. *Appl. Catal., A* **2003**, 246, 137–150.